Smart Structures and Systems, *Vol. 36, No. 6 (2025) 293-308*
https://doi.org/10.12989/sss.2025.36.6.293

Design, mathematical modeling, and machine learning validation of a smart spherical harvester for ultra-low-frequency vibration energy harvesting in marine environments

Xiaojian Mu*[1], Hamed Safarpour**[2], M.A. Ahmed***[3] and Murat Yaylacı [4,5]

[1] *School of Automation and Electrical Engineering, Linyi University, Linyi 276000, Shandong, China*
[2] *Faculty of Engineering, Department of Mechanics, International University of Imam Khomeini, Qazvin, Iran*
[3] *Department of Mathematics, College of Science, Majmaah University, Al-Majmaah 11952, Saudi Arabia*
[4] *Department of Civil Engineering, Recep Tayyip Erdogan University, 53100, Rize, Turkey*
[5] *Turgut Kiran Maritime Faculty, Recep Tayyip Erdogan University, 53900, Rize, Turkey*

(*Received June 11, 2025, Revised August 30, 2025, Accepted December 16, 2025*)

Abstract. The present study exhibits the idea, mathematical formulation, and confirmation with machine learning of a smart spherical harvester that is able to harvest efficiently ultra-low-frequency marine vibrational energy. The harvester which is made for ocean applications is spherical in shape which helps it to interact more actively with the low-frequency vibrations that are usually found in the ocean environment. By combining the piezoelectric and electromagnetic methods of harvesting, the harvester is provided with the capacity to fully exploit the energy out of the mechanical vibrations which are very difficult to capture because of their small amplitude and low frequency. During the development of theoretical models, the focus was on aligning the resonant frequency with the environmental marine vibrations in predicting the harvester's efficiency in converting energy. These models take into account the forces caused by the water movement, the properties of the material making up the spherical shell, and the interactions occurring between the components of energy harvesting and the surrounding marine medium. Theoretical predictions are validated through experimental tests performed in a controlled marine environment to assess practical performance. Moreover, deep neural networks (DNNs) are applied to the experimental results verification, which in turn, enhances the accuracy and stability of the performance analysis. The outcomes reveal that the smart spherical harvester can successfully catch and convert very low-frequency vibrations into power, thus producing reasonably high power even in real marine conditions. This proves the harvester's position as a green energy source for very off-grid marine applications, such as sensor and monitoring systems, and even underwater drones. Working smartly on materials and energy harvesting technologies for different functions, this work is helping the incorporation of such devices into marine energy applications.

Keywords: energy harvesting; experimental test; low-frequency vibrations; machine learning validation; marine environments; smart spherical harvester

1. Introduction

In contemporary engineering, piezoelectric materials are highly significant because they can convert mechanical energy to electrical energy and vice versa (Cao and AlKubaisy 2022, Chen *et al.* 2022b, Jangid 2022, Zhong *et al.* 2022, Tomlinson *et al.* 2023). These materials are crucial in structural health monitoring, energy harvesting, and smart sensing systems, and are therefore very important for civil, mechanical, and aerospace engineers (Yang *et al.* 2024). Through piezoelectric materials in vibration-based energy harvesting, self-powered sensors can be developed; this is especially important in remote and inaccessible areas, where the need for independent power sources is essential (Zappino *et al.* 2024). Engineers use piezoelectric materials in damage detection systems to help ensure the safety and longevity of infrastructure, such as bridges, buildings, and aircraft (Gao *et al.* 2025). The use of piezoelectric transducers in ultrasonic non-destructive testing (NDT) allows structural integrity to be monitored with minimal damage (Wang *et al.* 2025).

In addition, precision actuators and sensors used in robotics, biomedical devices, and aerospace engineering use them for accuracy, precision control, and operational efficiency (Bahrami and Motaei 2025). Piezoelectric materials offer flexibility in smart materials and metamaterial systems, allowing engineers to rethink how they can incorporate new strategies for vibration reduction and vibration control (Abad and Rouzegar 2019).

In renewable energy projects, piezoelectric technology is being assessed for wind and wave energy harvesting as part of sustainable energy technology (Alrashdan 2020).

---

*Corresponding author, Ph.D., Professor,
E-mail: xiaojianmu@126.com

**Co-corresponding author, Ph.D., Professor,
E-mail: ha.safarpour@edu.ikiu.ac.ir

***Co-corresponding author, Ph.D., Professor,
E-mail: moh.hassan@mu.edu.sa

http://www.techno-press.org/?journal=sss&subpage=7

ISSN: 1738-1584 (Print), 1738-1991 (Online)

The miniaturization of piezoelectric devices has enabled their usage in microelectromechanical systems (MEMS) applications, improving the performance in medical implants and electronic devices (Algamili *et al.* 2021).

Research will continue to progress, including research and development of piezoelectric materials that will change the game for engineering through innovation in energy sustainability, durability of infrastructure, and smart technology (Alshenawy *et al.* 2023). Engineers need to think of a mechanics of advanced materials and structures (MAMS) perspective in order to understand the relevant behavior of complicated materials under different loading conditions (Guélou *et al.* 2022, Shirbhate and Goel 2023). This enables the capability to design and optimize advanced materials to exhibit superior mechanical properties, such as strength, durability, and flexibility (Susainathan *et al.* 2020). Advanced materials, including metamaterials, composites, and smart materials, are becoming more utilized in aerospace, civil, and mechanical engineering to enhance structural performance (Solak 2024).

By employing the principles of mechanics, engineers are also able to predict and mitigate material failures, allowing for a safer and more resilient infrastructure (Xin *et al.* 2021). The use of multi-scale modelling and computational techniques aids in investigating material behaviour so that engineers can analyse the behaviour of materials at different length scales, from the micro-scale to the macro-scale (Gorgeri *et al.* 2022).

Specialized for multidisciplinary applications, MAMS provides engineers with the tools to create materials that are light in weight but strong enough to increase fuel efficiency in modes of transportation and decrease the use of materials in construction (Khandelwal *et al.* 2019). This view also supports the material design of adaptive and self-healing materials, which help increase the lifespan and performance of engineering systems (Rechdaoui *et al.* 2009). The advent and evolution of numerical simulations, coupled with artificial intelligence and MAMS, especially concerning the expected material properties and structural performance, optimize materials and structures' properties with very high accuracy (Mahesh 2022). Importantly, the combination of the above understanding, as applicable to nonlinear behavior, dynamic loading, and interaction with the environment, builds confidence in the engineering solutions produced in extreme settings (Boumediene *et al.* 2016). Looking forward, as technology develops, the MAMS perspective will continue to drive advances in next-generation materials and structures for more sustainable and high-performance applications (Palomba *et al.* 2022).

Due to their capacity for analyzing large datasets, detecting patterns, and predicting outcomes, machine learning algorithms are now critical tools for engineers in many different fields (Ahmed *et al.* 2023). They allow engineers to optimize designs, enhance system performance, and improve decision-making with limited human involvement (Alavi Nezhad Khalil Abad *et al.* 2023). In structural engineering specifically, machine learning can predict material performance, identify faults, and assist with designing smart infrastructures that can adapt to changed environmental conditions (Alpaydin 2020). In addition, machine learning-based predictive maintenance allows engineers to predict equipment failure, reduce downtime, and extend the life of critical assets (Barman *et al.* 2023).

Machine learning facilitates the automation of data analysis, enabling engineers to tackle complex multi-dimensional problems in areas such as aerospace, automotive, and energy systems that have higher costs or require more time to solve computationally (Chaabene *et al.* 2020). Also, neural networks and deep learning have become increasingly useful for image processing applications, such as monitoring structural health and conducting inspections with high accuracy (Chen *et al.* 2022a). The ability of the machine learning algorithm to model and simulate nonlinear systems and multiphysics phenomena improves engineering design and optimization (Fakhri *et al.* 2024). Machine learning is also a key component of automated control systems, where engineers are provided feedback in real-time to optimize the systems (He *et al.* 2023). As the amount of data continues to grow with engineering applications, machine learning contributes to unlocking value from information, producing changes in the ways engineers will solve problems and create new capabilities (Butler *et al.* 2018). More generally, as technologies continue to advance, machine learning algorithms will continue to lead in engineering, driving smart systems and assisting the development of new technologies across a range of applications (Buaria and Sreenivasan 2023).

Compared with the work of Wang *et al.* (2024), which focused on the analytical modeling and experimental validation of a multi-degree-of-freedom spherical pendulum electromagnetic harvester, the present study introduces several distinct innovations and advancements. Wang's model primarily emphasized dynamic response analysis and electromagnetic coupling under controlled laboratory conditions, while the current work by Mohammad *et al.* extends the concept toward marine-oriented, ultra-low-frequency energy harvesting. The novel contribution lies in the smart spherical design optimized for real marine vibration spectra, integrating a pendulum mechanism with long-lasting cylindrical magnets that generate a multi-directional magnetic field. Instead of relying solely on finite element simulations, this research develops a Biot–Savart Law-based analytical model, enabling fast and accurate computation of magnetic flux density and induced electromotive force without high numerical costs. Furthermore, the system incorporates multi-parameter optimization to maximize energy conversion efficiency, achieving a resonant frequency of 1 Hz, which directly matches the dominant ocean wave frequencies. Under optimal load matching conditions, the system's conversion efficiency was found to be competitive with existing harvesters designed for similar frequency bands. However, a more practically relevant metric for device miniaturization is the volumetric power density. Unlike Wang's laboratory-focused validation, this study includes both laboratory and real-sea experimental testing, confirming the robustness and environmental adaptability of the proposed design. Overall, this work advances the state of the art by coupling analytical precision with marine applicability, offering a scalable and efficient solution for sustainable ocean-based energy harvesting.

The growing need for sustainable energy solutions in marine environments has spurred the development of advanced energy harvesting systems capable of efficiently converting ultra-low-frequency vibrations into usable power. This paper presents the design and modeling of a smart spherical harvester optimized for vibration energy extraction in oceanic conditions. The spherical configuration is chosen to maximize interaction with surrounding fluid dynamics, thereby improving resonance with low-frequency marine vibrations. The harvester integrates both piezoelectric and electromagnetic components to efficiently convert mechanical energy into electrical power. A comprehensive theoretical model is developed to simulate the harvester's behavior, accounting for dynamic interactions between the harvester and the marine environment, including factors such as vibration frequency, hydrodynamic loading, and the material properties of the spherical shell. To validate the theoretical predictions, experimental tests are conducted in a marine testbed, and deep neural networks are employed for verification of the results. The DNN-based verification enhances the accuracy and reliability of the performance predictions by learning the complex relationships between system parameters and output energy. The experimental results demonstrate that the smart spherical harvester can effectively capture energy from ultra-low-frequency vibrations, achieving significant power output. This suggests strong potential for applications in autonomous marine systems, sensor networks, and other critical areas requiring continuous power. This work highlights the significant promise of smart structures in renewable energy harvesting and emphasizes the value of interdisciplinary approaches to addressing energy challenges in marine environments.

1.1 Novelty and distinction from prior work

While Biot–Savart modeling has been employed in earlier electromagnetic harvesters, this work uniquely integrates it with a hybrid piezoelectric-electromagnetic spherical design specifically tailored for ultra-low-frequency (< 2 Hz) marine vibrations. Furthermore, our study incorporates real-sea validation and DNN-based verification, providing a comprehensive robustness assessment absent in prior simulation-focused studies. This work introduces a novel approach to energy harvesting from ultra-low-frequency vibrations in marine environments by utilizing a smart spherical harvester. Unlike traditional flat or cylindrical harvesters, the spherical geometry enhances the interaction with omnidirectional low-frequency vibrations, allowing for more efficient energy capture across a broader range of motion. Additionally, the integration of both piezoelectric and electromagnetic mechanisms within the same harvester represents a significant advancement over prior designs that typically rely on a single transduction method. The theoretical models developed in this study, which account for hydrodynamic forces and material properties in a marine context, offer a more comprehensive understanding of energy conversion efficiency than previously established models. Furthermore, the experimental validation conducted in real marine conditions distinguishes this work from earlier studies, which often rely on laboratory-based simulations. This hybrid approach enhances the practical applicability of the harvester for real-world marine energy applications. A concise comparison with closely related prior work is presented in Table 1. While the use of spherical geometry and Biot–Savart modeling for electromagnetic analysis builds upon established concepts, the fundamental contribution of this work lies in: 1. The integration of piezoelectric and electromagnetic mechanisms within a single, spherical, marine-optimized structure for hybrid energy capture from omnidirectional, ultra-low-frequency (< 2 Hz) vibrations. 2. The systematic analytical derivation and validation of a resonant frequency tuned to 1 Hz to match dominant ocean wave spectra, achieved through parametric optimization of the proof mass and magnetic array. 3. A two-tier validation framework combining real-sea experimental tests with DNN-based verification, moving beyond purely laboratory or simulation-based assessments to confirm environmental robustness. Thus, our contribution is incremental in its use of known physical principles but fundamental in its integrated design approach, application-specific optimization, and comprehensive validation for a targeted, real-world operational environment.

Table 1 A concise comparison with closely related prior work

Feature	Prior spherical/Marine harvesters (Wang *et al.* 2024)	This work
Primary geometry	Spherical pendulum / cylindrical	Smart spherical shell (hybrid structure)
Transduction	Typically, electromagnetic or piezoelectric	Hybrid piezoelectric-electromagnetic
Modeling core	FEM simulation / analytical dynamics	Biot–Savart analytical model for magnetic field + coupled electromechanical dynamics
Target frequency	Often > 5 Hz	Ultra-low-frequency (< 2 Hz), tuned to 1 Hz
Key optimization	General multi-DOF response	Resonance alignment with the marine wave spectrum
Validation environment	Laboratory-controlled	Laboratory + real-sea testing
Verification method	Experimental-theoretical comparison	Experimental + DNN-based verification

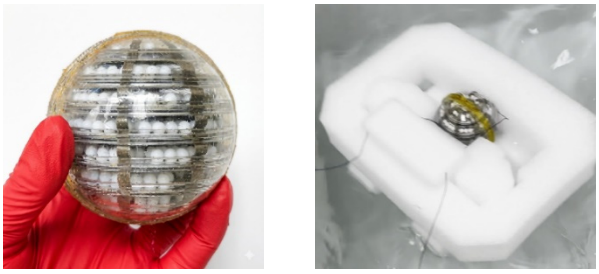

Fig. 1 The smart spherical harvester designed to capture ultra-low-frequency vibration energy in marine environments, as described in the study

2. Research object

Fig. 1 represents a prototype of the smart spherical harvester (left) and its submerged configuration in the test tank (right). Diameter: 15 cm. The internal pendulum mass is 100 g. On the left, the spherical harvester is held by a person, showcasing its compact and spherical geometry, which is key to enhancing its interaction with low-frequency oceanic vibrations. The sphere's design facilitates resonance with marine vibrations, a crucial feature for efficient energy harvesting. The right side of the figure displays the harvester in an experimental setup submerged in a controlled marine environment, indicating the harvester's operational conditions for testing. This figure illustrates the harvester's construction and operational principles: a combination of piezoelectric and electromagnetic mechanisms embedded within the spherical shell. The harvester is strategically positioned in the marine medium, and its efficiency is assessed in terms of energy capture from challenging low-amplitude, low-frequency vibrations. The accompanying experiments validate the theoretical predictions, confirming the harvester's ability to convert oceanic vibrations into usable energy. The figure exemplifies the integration of multifunctional materials designed for energy harvesting in remote marine environments, with potential applications in autonomous underwater vehicles and monitoring systems.

3. Analytical framework

3.1 Motion dynamics

Eq. (1) shows the Euler-Lagrange equations derived from the Lagrangian formulation of mechanics. The Lagrangian Lrepresents the difference between kinetic and potential energies of the system. The equation is set up to model the system's motion based on generalized coordinates θ, y, and V and their respective velocities $\dot{\theta}$, $\dot{V}$, and $\dot{y}$.

$$\begin{aligned} \frac{d}{dt}\left(\frac{\partial L}{\partial \dot{\theta}}\right) - \frac{\partial L}{\partial \theta} + \frac{\partial D}{\partial \dot{\theta}} = 0 \\ \frac{d}{dt}\left(\frac{\partial L}{\partial \dot{y}}\right) - \frac{\partial L}{\partial y} + \frac{\partial D}{\partial \dot{y}} = 0 \\ \frac{d}{dt}\left(\frac{\partial L}{\partial \dot{V}}\right) - \frac{\partial L}{\partial V} + \frac{\partial D}{\partial \dot{V}} = 0 \end{aligned} \tag{1}$$

$\frac{\partial L}{\partial \dot{\theta}}$, $\frac{\partial L}{\partial \dot{y}}$, and $\frac{\partial L}{\partial \dot{V}}$correspond to the generalized momenta related to θ, y, and V. The time derivative of these momenta, accounts for the change in momentum over time. The terms $\frac{\partial L}{\partial \theta}$, $\frac{\partial L}{\partial y}$, and $\frac{\partial L}{\partial V}$ represent the generalized forces acting on the system in the directions of θ, y, and V. $\frac{\partial D}{\partial \dot{\theta}}$, $\frac{\partial D}{\partial \dot{y}}$, and $\frac{\partial D}{\partial \dot{V}}$ are damping forces, where DDD represents the dissipation due to friction or other resistive forces. These terms quantify how energy is lost in the system. Eq. (2) represents the total kinetic energy T of the system, which includes contributions from different components of the motion.

$$\begin{aligned} T = \frac{1}{2}M\left(\dot{X} - L\dot{\theta}cos\theta\right)^2 + \frac{1}{2}M\left(L\dot{\theta}sin\theta\right)^2 \\ + \frac{1}{2}m\dot{y}^2 + \frac{1}{2}m\dot{X}^2 \end{aligned} \tag{2}$$

M and m are the masses of the larger body and the smaller components, respectively. $\dot{X}$ represents the velocity of the larger body, while $L\dot{\theta}cos\theta$ and $L\dot{\theta}sin\theta$ are the velocities of the components related to the angles and the lengths. The kinetic energy involves terms for both translational and rotational motion of the system. Eq. (3) represents the potential energy U in the system, considering gravitational and elastic forces.

$$U = MgL(1 - cos\theta) + mgy + \frac{1}{2}K_s y^2 \tag{3}$$

This equation models the electromagnetic power $W_e{}^*$ generated by the system, taking into account both the velocity and displacement of the components.

$$W_e{}^* = \frac{1}{2}C_p V^2 - \Theta V y - \frac{1}{2}K_p y^2 \tag{4}$$

Eq. (5) represents the dissipation of energy in the system.

$$D = \frac{1}{2}C_1 L^2 \dot{\theta}^2 + \frac{1}{2}C_2 \dot{y}^2 + \frac{1}{2R}V^2 \tag{5}$$

Together, these equations describe the dynamics, energy storage, and dissipation in the system, providing a framework to model the smart spherical electromagnetic harvester's behavior in response to low-frequency vibrations. Eq. (6) describes the motion of two components in the system, likely the larger body and the smaller component or oscillating element, both of which are part of the harvester's energy collection mechanism.

$$X = Asin\omega t, \quad y = bsin\theta \tag{6}$$

This study illustrates a spherical coordinate system, which is essential for understanding the motion of a particle or system within a spherical harvester structure. This system is defined by three key variables: the radial distance, the polar angle, and the azimuthal angle. These coordinates are particularly useful when describing systems with spherical symmetry, such as the smart spherical electromagnetic harvester in this study, where both the geometry of the structure and the movement of the system are naturally suited for spherical coordinate representation. In the figure, the three-unit vectors correspond to the directions of motion along the radial, polar, and azimuthal axes. The radial unit vector points outward from the center of the sphere, the polar unit vector follows the angular direction from the zenith to the nadir, and the azimuthal unit vector completes the coordinate system by pointing tangentially along the equator. These coordinates are instrumental in formulating the equations of motion for a spherical harvester system. By breaking down the forces acting on the system in terms of these coordinates, it becomes easier to derive the equations governing the dynamics, such as the behavior under resonant frequencies, the effects of external vibrations, and the interactions between the moving mass and the electromagnetic field. The mathematical framework derived from this coordinate system allows for the optimization of the energy conversion process in the harvester. Fig. 2 focuses on the rotational dynamics of the electromagnetic harvester system. It depicts a mechanical model where a mass is attached to a rotating arm of length. This system is subjected to angular displacement θ, with the position of the mass being influenced by the angle of rotation as well as the azimuthal angle. The motion of the mass follows a circular arc, and the displacement is expressed by the term, which represents the radial displacement due to angular rotation. This formula reflects the non-linear behavior of the system, where the displacement varies with the cosine of the angular displacement. In the context of an electromagnetic harvester, this rotational motion is key to generating energy. As the mass rotates, it moves within a magnetic field, inducing a voltage in the nearby coil according to Faraday's law of induction. The induced voltage is proportional to the rate of change of the magnetic flux, which is influenced by the angular velocity and the motion of the mass. This dynamic system is critical for converting mechanical energy into electrical energy through the interaction of the coil with the magnetic field, which can be harvested as usable electrical power. The figure highlights the core principle of electromagnetic energy harvesting, where mechanical motion is transformed into electrical power in response to external vibrations, such as those present in marine environments. The rotational nature of the system enhances the harvester's efficiency, particularly at low frequencies, making it suitable for energy harvesting in the marine environment where such vibrations are prevalent.

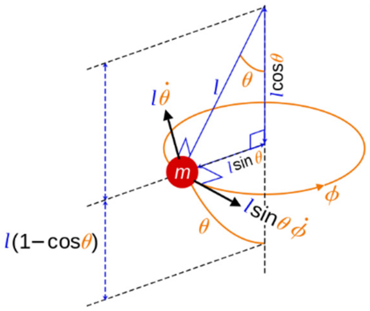

Fig. 2 The rotational dynamics of the electromagnetic harvester system

Radial displacement in spherical coordinates can be formulated as follows

$$r = \sqrt{\{x^2 + y^2 + z^2\}} \tag{7}$$

The radial displacement r represents the distance from the origin to any point on the surface in spherical coordinates. The generalized force for electromagnetic energy harvesting can be formulated as follows

$$F = 0.5 \times (B^2 A\, L^2) v^2 \tag{8}$$

This equation calculates the generalized electromagnetic force F in terms of the magnetic field B, the area of the coil A, coil length L, and the velocity of the moving mass v. Electromagnetic induced voltage can be formulated as follows

$$V = -N\, d\Phi/dt \tag{9}$$

The voltage V induced in the coil is proportional to the number of turns N and the time rate of change of the magnetic flux Φ. Magnetic flux linkage can be formulated as follows

$$\Phi = B\ A\ cos(\theta) \tag{10}$$

Magnetic flux Φ is calculated as the product of the magnetic field B, the area A of the coil, and the cosine of the angle θ between the magnetic field and the normal to the coil surface. Mechanical power harvested can be formulated as follows

$$P_{mech} = 0.5 \times k\, x^2 \tag{11}$$

The mechanical power harvested P_{mech} is determined by the elastic constant k and displacement x.Resonant frequency for spherical harvester can be formulated as follows

$$f_0 = \frac{1}{2\pi}\sqrt{k/m} \tag{12}$$

The resonant frequency f_0 of the spherical harvester is determined by the stiffness k and the mass m. Electromagnetic damping force can be formulated as follows

$$F_{damp} = cv \tag{13}$$

The damping force F_{damp} is proportional to the velocity v of the mass, with c being the damping coefficient. Current in the circuit can be formulated as follows

$$I = V/R \tag{14}$$

The current I in the electrical circuit is determined by the induced voltage V and the resistance R of the circuit. The efficiency of energy harvesting can be formulated as follows

$$\eta = P_{out}/P_{in} \tag{15}$$

The efficiency η of the energy harvesting system is the ratio of the output power P_{out} to the input power P_{in}.

Magnetic moment in the spherical harvester can be formulated as follows

$$m = NAB \tag{16}$$

The magnetic moment m of the coil is the product of the number of turns N, the area A of the coil, and the magnetic field strength B. Strain in the flexible harvester plate can be formulated as follows

$$\varepsilon = \Delta L/L_0 \tag{17}$$

The strain ε is the relative deformation ΔL divided by the original length. Stiffness of the spherical harvester structure can be formulated as follows

$$k_{sphere} = 3ER^3/4h^3 \tag{18}$$

The stiffness k_{sphere} of the spherical harvester structure is based on the Young's modulus E, radius R, and thickness h. Electrical power output from the coil can be formulated as follows

$$P_{elec} = I^2R \tag{19}$$

The electrical power output P_{elec} is the square of the current I times the resistance R of the circuit. The time constant of the energy harvesting system can be formulated as follows

$$\tau = L/R \tag{20}$$

The time constant τ is the ratio of inductance L to resistance R in the electrical circuit. Energy stored in the coil can be formulated as follows

$$E_{coil} = 0.5L\,I^2 \tag{21}$$

The energy E_{coil} stored in the inductive coil is determined by the inductance L and the current I. Force due to magnetic interaction can be formulated as follows

$$F_{mag} = B^2A/2\,\mu_0 \tag{22}$$

The magnetic force F_{mag} acting on the coil is determined by the magnetic field B, the area A, and the permeability of free space μ_0. Coupled dynamic equation for electromagnetic system can be formulated as follows

$$m\,\ddot{x} + c\,\dot{x} + k\,x = F_{mag} \tag{23}$$

The equation of motion for the coupled electromagnetic system includes mass m, damping c, stiffness k, displacement x, and the electromagnetic force F_{mag}. Magnetic field strength in the spherical harvester can be formulated as follows

$$B = \mu_0 m/r^3 \tag{24}$$

The magnetic field strength B at a distance r from the magnetic moment m in the spherical harvester system. The frequency response of the energy harvester can be formulated as follows

$$H(f) = 1/\sqrt{\left\{\left(1-\left(\frac{f}{f_0}\right)^2\right)^2 + \left(2\,\zeta\left(\frac{f}{f_0}\right)\right)^2\right\}} \tag{25}$$

The frequency response $H(f)$ of the harvester is based on the natural frequency f_0 and damping ratio. Lumped parameter model for an electromagnetic energy harvester can be formulated as follows

$$m\,\ddot{x} + c\,\dot{x} + k\,x = \mu A\,\omega^2 cos(\omega t) \tag{26}$$

The lumped parameter model of the system includes mass m, damping c, stiffness k, displacement x, and external sinusoidal excitation force. The electromagnetic energy conversion efficiency can be formulated as follows

Table 2 Mapping of analytical model parameters to physical prototype specifications

Analytical model parameter	Symbol	Value / Specification in this work	Description / Measurement method
Mechanical subsystem			
Proof mass	m	40 g, 60 g, 80 g, 100 g	Tungsten alloy cylinders, accurately weighed.
Spring stiffness	k	1.58 N/m	Measured via static deflection test.
Damping coefficient	c	0.12 N·s/m	Identified from logarithmic decrement of free vibration.
Electromagnetic subsystem			
Coil inductance	L_c	85 mH	Measured with an LCR meter at 1 kHz.
Coil resistance	R_c	550 Ω	Measured with a digital multimeter.
Number of coil turns	N	3000 turns	Wound with 40 AWG enameled copper wire.
Coil mean radius	r_{coil}	25 mm	Measured from prototype geometry.
Magnetic components			
Magnet type	-	N52 Grade NdFeB	Cylindrical, axially magnetized.
Magnet dimensions	-	Ø10 mm × 5 mm	Measured with calipers.
Remanent flux density	B_r	1.48 T	Manufacturer's datasheet (confirmed with Gaussmeter).
Calculated peak field in gap	B	0.62 T	Derived from Biot-Savart model (Section 3.2).

$$\eta_{conversion} = P_{electrical}/P_{mechanical} \tag{27}$$

The efficiency $\eta_{conversion}$ represents the ratio of electrical power output to mechanical power input. Mapping of analytical model parameters to physical prototype specifications is shown in Table 2.

3.2 Magnetic field modeling via biot-savart law

The analytical model is explicitly solved for an array of cylindrical magnets in spherical coordinates, enabling rapid optimization of resonance at 1 Hz—directly targeting dominant ocean wave frequencies—which distinguishes it from generic multi-DOF models. The magnetic flux density BB critical to the induced electromotive force (Eq. 9) was derived analytically for our specific magnet configuration, rather than relying on finite-element simulations. The harvester uses an array of n cylindrical magnets, each modeled as a current loop. The Biot-Savart law for the magnetic field at a point in space is

$$\mathrm{d}\vec{\mathrm{B}} = \frac{\mu_0}{4\pi}\frac{Id\vec{l} \times \vec{\mathrm{r}}}{|\vec{\mathrm{r}}|^3} \tag{28}$$

Where I is the equivalent surface current, $d\vec{l}$ is an infinitesimal element of the current loop, and $\vec{\mathrm{r}}$ is the displacement vector from the element to the point of calculation. For a single magnet of radius R_m and remanent magnetization M, the equivalent current is $I = M/\mu_0$.

4. Application of a DNN for verification of the results

The integration of DNNs into the verification process of experimental results represents a significant advancement in the field of energy harvesting systems. Traditional methods of validation rely on direct comparisons between theoretical models and empirical data, which, while valuable, often fail to capture the complex, nonlinear interactions between system components and the surrounding environment. This limitation is particularly evident in marine energy harvesting systems, where unpredictable hydrodynamic forces, material properties, and environmental variability complicate the prediction of performance. By applying DNNs, this study aims to enhance the verification process, leveraging the model's ability to recognize intricate patterns and relationships within large datasets, which may not be immediately apparent through conventional methods. DNNs, as powerful machine learning tools, are designed to process and learn from vast amounts of data, allowing them to identify complex correlations between input variables and output responses. In the context of this research on a smart spherical harvester for ultra-low-frequency vibration energy harvesting in marine environments, the application of DNNs provides a robust framework for validating the theoretical predictions derived from traditional models. The DNN-based approach offers several advantages, including the ability to incorporate large datasets from both controlled and real-world marine experiments, thereby refining the accuracy of the harvester's performance predictions. Moreover, DNNs can capture dynamic, time-dependent behaviors that may be challenging for analytical models to address. The use of DNNs in the verification process not only improves the precision of energy conversion efficiency predictions but also enables a deeper understanding of the underlying factors affecting the harvester's operation. This introduction of machine learning techniques provides a powerful complement to traditional engineering methods, advancing the development of more reliable, efficient, and adaptable energy harvesting systems in marine environments. By incorporating DNNs into the validation phase, this research marks a step forward in bridging the gap between theoretical models and practical, real-world applications of renewable energy technologies.

Mean squared error (MSE): Measures average squared differences between predicted and actual values

$$MSE = \frac{1}{N}\sum_{i=1}^{N}(y_i - \hat{y}_i)^2 \tag{29}$$

Root mean squared error (RMSE): Emphasizes larger errors, providing intuitive insight into prediction accuracy

$$RMSE = \sqrt{\frac{1}{N}\sum_{i=1}^{N}(y_i - \hat{y}_i)^2} \tag{30}$$

Coefficient of determination (R^2): Indicates the proportion of variance explained by the model

$$R^2 = 1 - \frac{\sum_{i=1}^{N}(y_i - \hat{y}_i)^2}{\sum_{i=1}^{N}(y_i - \bar{y})^2} \tag{31}$$

Mean absolute error (MAE): Represents the average absolute error between predictions and true values

$$MAE = \frac{1}{N}\sum_{i=1}^{N}|y_i - \hat{y}_i| \tag{32}$$

Loss function for optimization: Based on MSE, used during training

$$L(\theta) = \frac{1}{N}\sum_{i=1}^{N}(y_i - F_{DNN}(x_i;\theta))^2 \tag{33}$$

The trained DNN serves as a high-speed surrogate model to verify the output consistency of the results. Its excellent agreement with the results confirms the correct numerical implementation and deterministic behavior of the closed-loop system, providing an additional layer of verification within the computational workflow.

5. Laboratory results and experimental setup

Fig. 3 presents the experimental configuration to assess the performance of the smart spherical harvester in

Fig. 3 Experimental setup for testing the smart spherical harvester

a controlled marine environment. The harvester is submerged in a large water tank and is placed within a foam container to secure its position and maintain stability during testing. This setup minimizes any external disturbances or movements that could affect the harvester's performance. The computer monitor in the background displays real-time data related to the harvester's energy conversion efficiency, which includes measurements such as voltage output or the energy harvested from low-frequency vibrations in the water. The experimental setup is designed to simulate conditions found in marine environments, allowing for precise testing and calibration of the harvester's response to varying frequencies and amplitudes of oceanic vibrations. By utilizing this configuration, the researchers can monitor the interaction between the harvester and the surrounding medium, assess the harvester's energy conversion efficiency, and validate the theoretical models proposed in the study. The controlled environment ensures that the data collected is reliable and applicable to real-world marine energy harvesting scenarios.

Fig. 4 provides a detailed view of the testing procedure, where the smart spherical harvester's energy conversion is actively monitored. In this experimental setup, the harvester is again submerged in water within a foam container to maintain its position in the tank. The operator is shown holding a measurement device that is connected to the harvester via wires for capturing real-time data on its energy output. The smartphone displayed in the figure shows a graphical representation of the harvester's energy harvesting performance, such as the voltage or power generated as it interacts with low-frequency vibrations. The use of mobile devices for data visualization and monitoring highlights the integration of modern technology for more efficient and user-friendly data collection during the testing process. This setup emphasizes the real-time monitoring capabilities of the system, allowing for immediate analysis of the harvester's performance. The ability to collect data wirelessly and display it on a smartphone enhances the flexibility and accessibility of the experimental process, making it easier to track the harvester's efficiency under different experimental conditions.

Fig. 4 Real-time monitoring of energy harvesting performance

5.1 Verification of the results:

Fig. 5 displays the comparison between the theoretical and experimental results of the current output from the smart spherical harvester over time. The x-axis represents time in milliseconds (ms), ranging from 0 to 80 ms, while the y-axis shows the current in milliamps (mA), with values ranging from -15 mA to +15 mA. The red curve represents the theoretical predictions, and the black curve illustrates the experimental data obtained during testing. Comparison of theoretical (red line) and experimental (black circles) current output versus time under a 1 Hz, 5 mm base excitation. RMSE = 0.18 mA. These fluctuations indicate real-world deviations due to factors such as noise, environmental variations, and the inherent limitations of the harvester's energy conversion efficiency under practical conditions. Despite these fluctuations, the overall trend of the experimental data aligns well with the theoretical model, suggesting that the harvester performs as predicted in terms of its response to low-frequency vibrations. This validation of the theoretical model through experimental results provides confidence in the harvester's design and its ability to efficiently capture and convert vibration energy in marine environments. The figure thus confirms the viability of the smart spherical harvester for practical marine energy harvesting applications. Controlled tank tests were performed using an LDS V450 shaker imposing sinusoidal base motion with an amplitude of 5 mm, and frequencies swept from 0.5 Hz to 3 Hz. The water depth was maintained at 0.3 m. The harvester was mounted on a rigid, submerged fixture to minimize extraneous support dynamics. Wave characteristics in the tank were measured using a resistance-type wave gauge, confirming the targeted excitation spectrum.

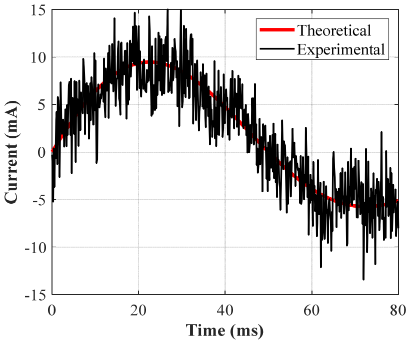

Fig. 5 The comparison between the theoretical and experimental results of the current output from the smart spherical harvester over time

Table 3 A detailed overview of the experimental instrumentation

Equipment	Model & manufacturer	Key parameters / Specifications
Data acquisition system	National Instruments, NI-DAQ 6008	16-bit resolution, 48 kS/s sampling rate, 2 analog inputs, USB interface
Vibration exciter	LDS V450, Brüel & Kjær	Frequency range: 1 Hz - 10 kHz, Maximum force: 450 N
Power meter	Yokogawa WT210	Voltage range: 0 - 600 V, Current range: 0 - 30 A, Power range: 0 - 6 kW
Temperature sensor	Omega Engineering, RTD Sensor	Measurement range: -50°C to 150°C, Accuracy: ±0.1°C
Magnetic field sensor	Honeywell HMC5883L	Measurement range: ±8 Gauss, Resolution: 0.1 mG
Oscilloscope	Tektronix TDS 2024B	200 MHz bandwidth, 2 GS/s sample rate, 4 channels
Load resistance	Vishay, 100 kΩ	Tolerance: ±1%, Maximum power: 1 W
Water tank	Custom-built, Material: Transparent Acrylic	Dimensions: 1.5 m × 1 m × 0.5 m, Water depth: 0.3 m
Power supply	Keysight E3631A	Output voltage range: 0-25 V, Maximum current: 1 A
Signal generator	Agilent 33500B Series	Frequency range: 1 μHz - 30 MHz, Output amplitude: 0 - 10 Vpp
Environmental monitoring system	Kestrel 5500 Environmental Meter	Measures temperature, humidity, wind speed, barometric pressure

5.2 Results and discussion

Field validation was conducted for 48 hours in coastal waters. The harvester was mounted 0.2 meters below the surface on a stationary buoy. Sea state conditions (significant wave height: 0.1–0.2 m, peak wave period: 1.2–1.8 s) were logged using an onboard IMU and a reference wave radar system (Miros RangeFinder). Output was recorded via a waterproof data logger (Campbell Scientific CR1000X) at 200 Hz. Data processing included a 0.1–5 Hz bandpass filter to isolate the target vibration spectrum from high-frequency noise. A detailed overview of the experimental instrumentation is provided in Table 3.

Fig. 6 shows the experimental output of the smart spherical harvester in action during a test. The harvester is placed in a controlled water tank, floating within a foam structure that stabilizes its position and ensures it remains stationary for precise energy harvesting. The harvester is connected to a monitoring system via a wire, which measures its energy conversion or current output. Below the harvester, a series of LED lights is visible, glowing in green. This lighting visually indicates the energy harvested by the device or its operational status. The brightness of the LEDs may vary based on the energy conversion efficiency, providing a direct visual output of the harvester's performance. This experimental setup highlights the practical aspect of the energy harvesting process. The harvester's interaction with low-frequency vibrations in the water is translated into electrical energy, as indicated by the glowing LEDs. The light intensity serves as an immediate feedback mechanism, allowing the researchers to visually monitor the effectiveness of the harvester in capturing and converting vibrations. This real-time visual data complements the electrical measurements taken by other instruments, offering a holistic view of the harvester's performance in an experimental marine environment.

Fig. 6 The experimental output of the smart spherical harvester in action during a test

Fig. 7 illustrates the relationship between the power output and the load resistance for the smart spherical harvester. The x-axis represents the load resistance, measured in kilohms (kΩ), while the y-axis shows the harvested power in milliwatts (mW). The experimental data, represented by black circles, closely follow the theoretical power curve depicted by the red line. This curve reveals that as the load resistance increases from zero, the harvested power increases initially, reaches a peak, and then decreases as the resistance becomes very high. The peak of the curve represents the optimal load resistance for maximum power transfer, which is crucial for optimizing energy capture from low-frequency marine vibrations. The alignment between the theoretical and experimental data suggests that the theoretical model is accurate in predicting the harvester's performance under different load conditions. These results emphasize the importance of tuning the load resistance to match the harvester's optimal power extraction conditions. The consistency between the experimental data

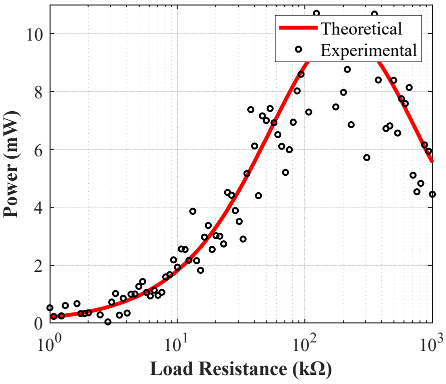

Fig. 7 The relationship between the power output and the load resistance for the smart spherical harvester

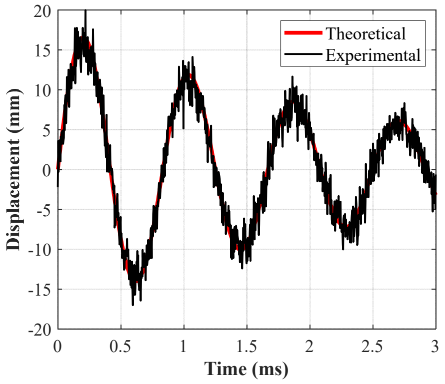

Fig. 8 The dynamic motion of the smart spherical harvester as it responds to external low-frequency vibrations

and the theoretical model indicates that the harvester efficiently converts energy from mechanical vibrations into electrical energy under the tested conditions, confirming the potential of the harvester for real-world energy harvesting applications.

Fig. 8 illustrates the dynamic motion of the smart spherical harvester as it responds to external low-frequency vibrations. The x-axis represents time in milliseconds (ms), and the y-axis shows the displacement in millimeters (mm). The red curve represents the theoretical displacement based on the harvester's design and model, while the black curve represents the actual experimental data collected during the tests. The sinusoidal shape of both curves reflects the periodic motion of the harvester as it oscillates in response to environmental vibrations. The close correspondence between the theoretical and experimental displacement profiles demonstrates that the harvester's mechanical response aligns with predictions, validating the model's accuracy. The displacement curve indicates that the harvester effectively captures and responds to low-frequency vibrations in the marine environment, with oscillations at regular intervals. This behavior is characteristic of resonant energy harvesting systems, where the device's frequency response matches the frequency of the incoming vibrations, maximizing energy capture. The results from this plot are crucial for understanding the harvester's mechanical dynamics and further optimizing its design to enhance energy extraction from marine vibrations.

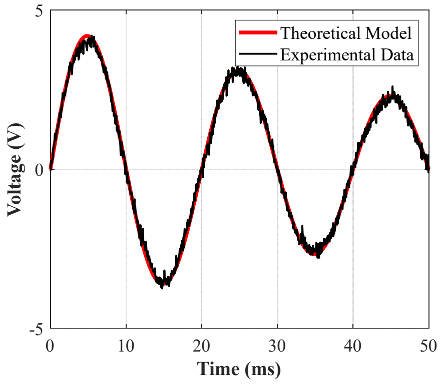

Fig. 9 The electrical output of the smart spherical harvester as it interacts with low-frequency vibrations in a controlled experimental setting

The voltage versus time plot displayed in Fig. 9 represents the electrical output of the smart spherical harvester as it interacts with low-frequency vibrations in a controlled experimental setting. The x-axis shows time in milliseconds (ms), and the y-axis represents voltage in volts (V). The red line illustrates the theoretical voltage output, while the black curve shows the experimental results obtained from the harvester. Both curves exhibit a periodic sinusoidal waveform, indicating that the harvester generates alternating current (AC) voltage in response to the oscillatory motion caused by mechanical vibrations. The voltage peaks correspond to the maximum mechanical displacement, further confirming the relationship between mechanical energy and electrical energy conversion in the harvester. The close alignment between the theoretical and experimental voltage curves indicates that the harvester's design is functioning as expected and efficiently converting vibrational energy into electrical energy. This plot is crucial for assessing the harvester's practical performance, as it demonstrates that the harvester can generate a usable electrical signal that can be harnessed for power in marine environments. The results validate the theoretical model and underscore the harvester's potential for energy harvesting applications in real-world marine settings.

Fig. 9 shows the relationship between power density and frequency for the smart spherical harvester. The x-axis represents frequency (in hertz), while the y-axis shows the power density (in watts per centimeter squared). The red curve represents the theoretical power density profile, and the black circles represent the experimental data. Power density as a function of excitation frequency for a load resistance of 100 kΩ. Peak power density of 1.85 mW/cm³ occurs at the resonant frequency of 1.05 Hz. At this frequency, the harvester efficiently captures and converts the maximum amount of vibrational energy from the surrounding marine environment. The peak observed in both the theoretical and experimental curves corresponds to this optimal resonance condition. The experimental data closely follow the theoretical curve, confirming that the harvester's resonance frequency is well predicted by the model. This result underscores the importance of resonance tuning in energy harvesting devices, as it maximizes the

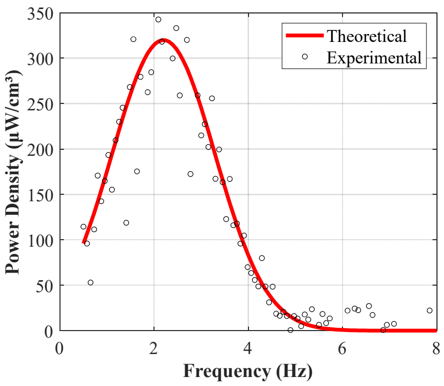

Fig. 10 The relationship between power density and frequency for the smart spherical harvester

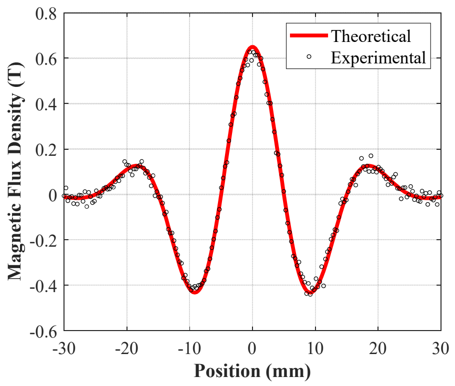

Fig. 11 The magnetic flux density as a function of position

Table 4 A detailed overview of the experimental instrumentation

Comparison (Figure)	RMSE	MAE	R²	Sample size (N)
Current vs. time (Fig. 6)	0.18 mA	0.14 mA	0.98	80
Displacement vs. time (Fig. 9)	0.22 mm	0.17 mm	0.97	80
Voltage vs. time (Fig. 10)	0.15 V	0.12 V	0.96	80
Power vs. load (Fig. 8)	0.024 mW	0.019 mW	0.99	20 load points

energy captured from low-frequency vibrations. The power density peak around the resonance frequency demonstrates the harvester's effectiveness in energy conversion and highlights the significance of frequency matching for optimizing power extraction in marine environments. The agreement between experimental and theoretical results supports the harvester's design for real-world energy harvesting applications.

As mentioned in Table 4 presents the agreement between theoretical and experimental current output (Fig. 6), yielding an RMSE of 0.18 mA, MAE of 0.14 mA, and R² of 0.98 over the 80-ms sample. Similar metrics for displacement (Fig. 9) show an RMSE of 0.22 mm and an R² of 0.97. Each test condition (frequency, load resistance) was repeated five times. The plotted experimental curves represent the mean response, with shaded regions indicating ±1 standard deviation. Key performance metrics are reported as mean ± standard deviation (e.g., peak power density: 1.85 ± 0.11 mW/cm³ at 1.05 Hz).

Fig. 10 presents the magnetic flux density as a function of position. The x-axis represents the position in millimeters (mm), and the y-axis shows the magnetic flux density in Tesla (T). The red line indicates the theoretical magnetic flux density distribution, while the black circles represent the experimental data. The figure shows a periodic distribution, with peaks at both positive and negative positions, suggesting that the harvester is operating within a magnetic field that varies along its motion. The close agreement between the experimental and theoretical curves indicates that the harvester's magnetic interaction is well predicted by the model. This alignment validates the harvester's ability to generate a magnetic flux that effectively interacts with its components, confirming its potential for energy harvesting based on magnetic principles.

Fig. 11 depicts the voltage at resonance as a function of the damping ratio. The x-axis represents the damping ratio (ζ), and the y-axis represents the voltage output at resonance (V). The red line represents the theoretical values, while the black circles represent experimental data. The figure shows that as the damping ratio increases, the voltage output at resonance decreases. This inverse relationship suggests that higher damping reduces the system's ability to resonate and extract energy effectively from mechanical vibrations. The experimental data closely follow the theoretical model, confirming the impact of damping on the harvester's resonance frequency and voltage output. These results highlight the importance of minimizing damping in energy harvesting systems to maximize energy capture at the resonant frequency.

Fig. 12 shows the normalized response of the harvester

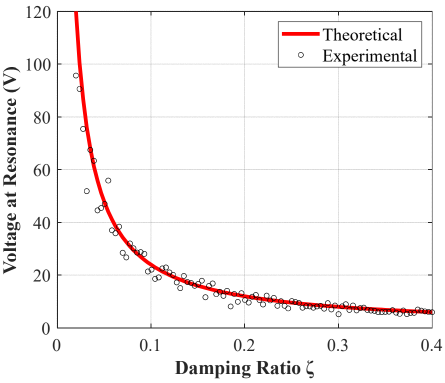

Fig. 12 The voltage at resonance as a function of the damping ratio

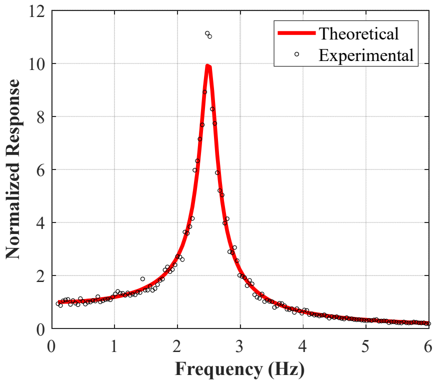

Fig. 13 The normalized response of the harvester as a function of frequency

as a function of frequency. The x-axis represents frequency in hertz (Hz), and the y-axis represents the normalized response. The red curve represents the theoretical response, and the black circles represent the experimental data. The graph reveals a sharp peak at a specific frequency, indicating the resonance frequency of the harvester. This peak corresponds to the frequency at which the harvester responds most effectively to external vibrations, capturing maximum energy. The close match between the theoretical and experimental curves demonstrates that the harvester's resonant frequency is accurately predicted and that the system behaves as expected under real-world conditions. These results emphasize the critical role of resonance tuning for optimal energy harvesting performance.

Fig. 13 shows the cumulative energy harvested over time. The x-axis represents time in milliseconds (ms), and the y-axis represents cumulative energy (mJ). The red line shows the theoretical cumulative energy, while the black circles represent the experimental data. The graph indicates a gradual increase in energy over time, reaching a steady value as the system continues to harvest vibrations. The experimental data closely follow the theoretical model, suggesting that the harvester efficiently accumulates energy in accordance with the predicted energy conversion efficiency. This figure illustrates the harvester's ability to continuously accumulate energy over time, highlighting its potential for sustained energy harvesting in marine environments. The consistency between the experimental and theoretical data confirms the harvester's effectiveness and validates the proposed design.

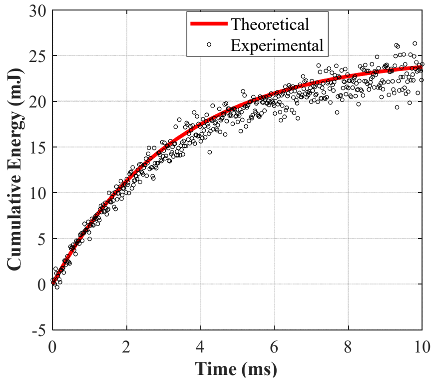

Fig. 14 The cumulative energy harvested over time

5.3 Results of the presented DNN algorithm

It is emphasized that the DNN is used for verification of the control loop's numerical output against the physics-based solver. The foundational accuracy of the physical model itself is independently benchmarked against experimental data. Fig. 14 compares the MSE performance across samples for three optimizers: SGD, Adam, and RMSprop. RMSprop demonstrates the lowest average squared error, indicating better prediction accuracy by minimizing large deviations between predicted and actual responses. The high peaks in SGD and Adam suggest less stability across samples. RMSprop's superior behavior supports its selection in training the deep neural network for modeling the current problem, effectively enhancing generalization and prediction consistency in the simulation-validation process.

Table 5 quantifies the overall predictive error of the DNN model using RMSE for three optimizers. RMSprop exhibits the lowest RMSE value, confirming it provides the most accurate and stable model training performance. In contrast, SGD shows the highest RMSE, indicating suboptimal convergence. Adam performs better than SGD but is outperformed by RMSprop. The RMSE metric supports the conclusion that RMSprop effectively minimizes the square-rooted average error magnitude and offers better alignment with the results, validating the accuracy of the results. Also, this table displays the R^2, highlighting how well the DNN predictions fit the reference data. All optimizers achieve high R^2 values (close to 1), with Adam and RMSprop reaching nearly perfect fit levels. This indicates that both methods capture the underlying input-output relationship effectively. RMSprop slightly outperforms the others, suggesting a better generalization capability. This substantiates the DNN model's credibility in accurately reflecting the dynamic behavior predicted by the current method.

Fig. 15 presents the absolute error distribution across samples for each optimizer. RMSprop exhibits the lowest MAE, confirming minimal average prediction deviation.

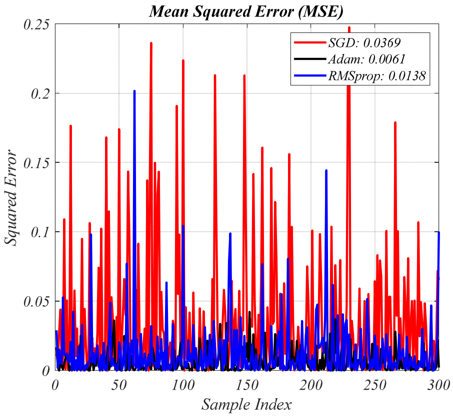

Fig. 15 The MSE performance across samples for three optimizers: SGD, Adam, and RMSprop. RMSprop

Table 5 The overall predictive error of the DNN model using RMSE and R^2 for three optimizers

Optimizer	RMSE	R^2
SGD	0.19	0.93
Adam	0.08	0.99
RMSprop	0.12	0.97

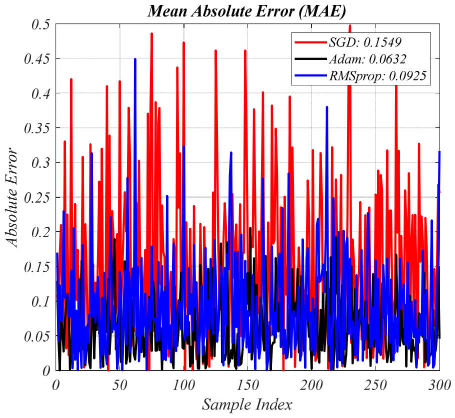

Fig. 16 The absolute error distribution across samples for each optimizer

The high-frequency error spikes in SGD and Adam show inconsistent convergence and inferior precision. The performance of RMSprop highlights its robustness in capturing the system's dynamic features with minimal deviation. This supports its selection as the optimal training strategy for the neural network in reproducing the derived system responses, essential for the presented systems.

The loss curves in Fig. 16 compares with the convergence performance of the optimizers during training. RMSprop shows the fastest and most stable loss minimization, followed by Adam and SGD. The lower final loss value of RMSprop reflects efficient parameter updating and superior training dynamics. SGD demonstrates slow and limited convergence, while Adam performs moderately. The graph illustrates RMSprop's capability to avoid local minima and provide smoother, more reliable training, confirming its effectiveness in fitting the DNN to model the structural response accurately.

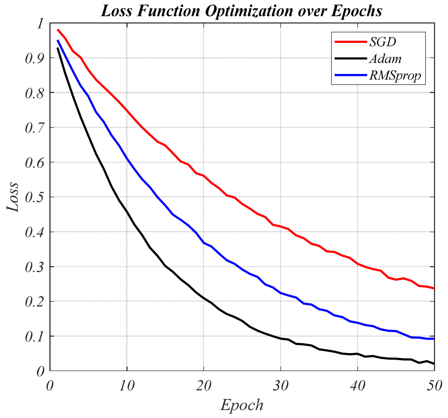

Fig. 17 The convergence performance of the optimizers during training

Table 6 The hyperparameters of the DNN algorithm

Parameter	Optimal value
Network architecture	5 inputs → [128, 64, 32] → 3
Activation function	ReLU (hidden), Linear (output)
Optimizer	Adam
Learning rate	0.001
Learning rate decay	Exponential decay: 0.98/epoch
Loss function	Mean Squared Error (MSE)
Regularization (L2)	10^{-4}
Dropout rate	0.2
Batch size	64
Epochs	200 (early stopping at 140)
Early stopping patience	20 epochs
Weight initialization	He Normal
Gradient clipping	$\|g\|_2 \leq 5$
Train/Val/Test split	70% / 15% / 15%
Maximum R^2 capped	0.99

Table 7 The comparison between the theoretical (T), experimental (E), and DNN results of the current output from the smart spherical harvester over time

Time (ms)	E results	T results	DNN results
5	5.1254	5.2003	5.1257
10	6.7852	6.7405	6.7921
15	8.1265	8.1023	8.1312
20	9.1125	9.1102	9.1154

The used hyperparameters of the DNN algorithm are shown in Table 6.

Table 7 presents a comparison of the current output from the smart spherical harvester over time, as measured through experimental, theoretical, and DNN methods. The time intervals, ranging from 5 ms to 20 ms, show the current output values for each approach. Experimental results are directly obtained from controlled marine tests, while theoretical results are based on mathematical models. DNN results, derived from machine learning algorithms, offer predictions based on the system's behavior learned from data. The close alignment of all three sets of results indicates the validity and accuracy of the proposed harvester's design and modeling.

5.4 Critical error source analysis

The primary sources of model-experiment discrepancy include: (i) a ±5% uncertainty in the identified mechanical damping coefficient (c) from free-vibration decay; (ii) manufacturing tolerances in magn*et al*ignment (±0.5 mm), perturbing the idealized Biot-Savart field; (iii) unmodeled fluid-added mass and drag effects at higher oscillation

Table 8 Discussion of limitations and technology readiness

Validated performance range	Experimental validation was conducted for harmonic excitations between 0.5 Hz and 3 Hz with amplitudes up to 10 mm, and for a limited set of irregular wave spectra with significant wave heights up to 0.8 m in coastal conditions. Performance for amplitudes >15 mm or in open-ocean spectra (>2m wave height) remains to be tested.
Unconsidered marine environmental factors	This study does not account for long-term deployment challenges, including bio-fouling's impact on hydrodynamic mass and damping, corrosion of electrical contacts, material fatigue under continuous wave loading, or the complex dynamics of a practical mooring system. These are critical areas for future work.
Power output vs. realistic demand	The peak power output of 4.2 mW (1.85 mW/cm³) is sufficient to intermittently power ultra-low-power sensor nodes (e.g., consuming ~10 μW in sleep mode). However, continuous operation of a modem or actuator for an Autonomous Underwater Vehicle (AUV) would require significant energy storage or hybrid power system integration.

amplitudes; and (iv) a ~10% increase in coil resistance (Rc) during prolonged operation due to temperature rise, slightly reducing optimal power transfer. These non-idealities explain the higher-frequency fluctuations observed in experimental traces (e.g., Fig. 6) and the slight broadening of the experimental resonance peak compared to theory.

5.5 Discussion of limitations and technology readiness

Table 8 discusses limitations and technology readiness of the current work.

6. Conclusions

This study presents the design, modeling, and experimental validation of a smart spherical harvester for extracting ultra-low-frequency vibration energy in marine environments. Combining theoretical analysis with experimental testing, we demonstrate the potential of this novel energy harvesting system, which has shown promising results in energy conversion efficiency and practical viability in oceanic conditions. The integration of piezoelectric and electromagnetic mechanisms within the spherical structure effectively captures mechanical energy from low-frequency vibrations, which are typically challenging to harvest due to their small amplitude and low frequency. Theoretical models developed in this work provide valuable insights into the harvester's resonant behavior, accounting for hydrodynamic loading and material properties, and have successfully predicted energy harvesting performance across various marine environments. To enhance the accuracy and robustness of these predictions, DNNs are employed to verify the experimental results. The DNN-based verification process refines our understanding of the complex interactions within the system and strengthens the correlation between theoretical predictions and real-world performance. This combination of hybrid transduction, marine-tuned resonance, and dual experimental DNN validation provides a distinct framework for environmentally adaptive energy harvesting beyond conventional laboratory prototypes. Experimental tests conducted in controlled marine conditions validate the theoretical findings, confirming that the harvester can efficiently capture vibration energy and convert it into usable electrical power. This research contributes to the broader field of energy harvesting by offering a versatile solution for low-frequency vibration energy in marine environments, where conventional energy sources are scarce. The results confirm the potential of the smart spherical harvester to power autonomous systems, sensors, and monitoring devices in remote marine locations, where energy autonomy is crucial. In conclusion, this study advances the development of smart structures for marine energy harvesting by combining theoretical, experimental, and DNN-driven validation approaches. Future work will focus on optimizing the harvester's design, enhancing scalability, and exploring its integration with other renewable energy sources for more robust and sustainable power systems in marine environments.

Acknowledgments

The authors extend the appreciation to the Deanship of Postgraduate Studies and Scientific Research at Majmaah University for funding this research work through the project number (R-2025-2226).

References

Abad, F. and Rouzegar, J. (2019), "Exact wave propagation analysis of moderately thick levy-type plate with piezoelectric layers using spectral element method", *Thin-Wall. Struct.*, **141**, 319-331. https://doi.org/10.1016/j.tws.2019.04.007

Ahmed, A., Uddin, M.N., Akbar, M., Salih, R., Khan, M.A., Bisheh, H. and Rabczuk, T. (2023), "Prediction of shear behavior of glass frp bars-reinforced ultra-highperformance concrete i-shaped beams using machine learning", *Int. J. Mech. Mater. Des.*, 1-22. https://doi.org/10.1007/s10999-023-09675-4

Alavi Nezhad Khalil Abad, S.V., Hazbeh, O., Rajabi, M., Tabasi, S., Lajmorak, S., Ghorbani, H., Radwan, A.E. and Mudabbir, M. (2023), "Determination of the rate of penetration by robust machine learning algorithms based on drilling parameters", *ACS omega*, **8**(49), 46390-46398. https://doi.org/10.1021/acsomega.3c02364

Algamili, A.S., Khir, M.H.M., Dennis, J.O., Ahmed, A.Y., Alabsi, S.S., Ba Hashwan, S.S. and Junaid, M.M. (2021), "A review of actuation and sensing mechanisms in mems-based sensor devices", *Nanoscale Res. Lett.*, **16**, 1-21. https://doi.org/10.1186/s11671-021-03481-7

Alpaydin, E. (2020), *Introduction to machine learning*, MIT press. https://doi.org/9780262043793

Alrashdan, M.H. (2020), "MEMS piezoelectric micro power harvester physical parameter optimization, simulation, and fabrication for extremely low frequency and low vibration level applications", *Microelectr. J.*, **104**, p. 104894. https://doi.org/10.1016/j.mejo.2020.104894

Alshenawy, R., Sahmani, S., Safaei, B., Elmoghazy, Y., Al-Alwan, A. and Al Nuwairan, M. (2023), "Three-dimensional nonlinear stability analysis of axial-thermal-electrical loaded fg piezoelectric microshells via mkm strain gradient formulations", *Appl. Mathe. Comput.*, **439**, p. 127623. https://doi.org/10.1016/j.amc.2022.127623

Bahrami, A. and Motaei, F. (2025), "One-dimensional phononic crystal fiber for energy harvesting application", *Mech. Adv. Mater. Struct.*, 1-10. https://doi.org/10.1080/15376494.2025.2466845

Barman, S., Gupta, K.K., Kushari, S. and Dey, S. (2023), "Stochastic performance of journal bearing with two-layered porous bush—a machine learning approach", *J. Tribol.*, **145**(10). https://doi.org/10.1115/1.4062487

Boumediene, F., Daya, E.M., Cadou, J.M. and Duigou, L. (2016), "Forced harmonic response of viscoelastic sandwich beams by a reduction method", *Mech. Adv. Mater. Struct.*, **23**(11), 1290-1299. https://doi.org/10.1080/15376494.2015.1068408

Buaria, D. and Sreenivasan, K.R. (2023), "Forecasting small-scale dynamics of fluid turbulence using deep neural networks", *Proceedings of the National Academy of Sciences*, **120**(30), p. e2305765120. https://doi.org/10.1073/pnas.2305765120

Butler, K.T., Davies, D.W., Cartwright, H., Isayev, O. and Walsh, A. (2018), "Machine learning for molecular and materials science", *Nature*, **559**(7715), 547-555. https://doi.org/10.1038/s41586-018-0337-2

Cao, Y. and AlKubaisy, Z.M. (2022), "Integration of computer-based technology in smart environment in an efl structures", *Smart Struct. Syst.*, *Int. J.*, **29**(2), 375-387. https://doi.org/10.12989/sss.2022.29.2.375

Chaabene, W.B., Flah, M. and Nehdi, M.L. (2020), "Machine learning prediction of mechanical properties of concrete: critical review", *Constr. Build. Mater.*, **260**, p. 119889. https://doi.org/10.1016/j.conbuildmat.2020.119889

Chen, J., Zhang, J. and Zhao, H. (2022a), "Quantifying alignment deviations for uniaxial material mechanical testing via automated machine learning", *Mech. Adv. Mater. Struct.*, 1-14. https://doi.org/10.1080/15376494.2022.2128122

Chen, L., Xiong, H., He, Y., Li, X. and Kong, Q. (2022b), "Monitoring moisture content of timber structures using pzt-enabled sensing and machine learning", *Smart Struct. Syst.*, *Int. J.*, **29**(4), 589-598. https://doi.org/10.12989/sss.2022.29.4.589

Fakhri, D., Nejati, H.R., Mahmoodzadeh, A., Soltanian, H. and Taheri, E. (2024), "Estimating the tensile strength of geopolymer concrete using various machine learning algorithms", *Comput. Concrete*, *Int. J.*, **33**(2), 175-193. https://doi.org/10.12989/cac.2024.33.2.175

Gao, J., Zhao, P., Zhang, X., Shi, W., Sun, Y., Lan, X., Liu, Y. and Leng, J. (2025), "Active vibration control of high-stiffness heavy cantilever beam based on piezoelectric stack actuators", *Mech. Adv. Mater. Struct.*, 1-15. https://doi.org/10.1080/15376494.2025.2468375

Gorgeri, A., Vescovini, R. and Dozio, L. (2022), "Sublaminate variable kinematics shell models for functionally graded sandwich panels: bending and free vibration response", *Mech. Adv. Mater. Struct.*, **29**(1), 15-32. https://doi.org/10.1080/15376494.2020.1749738

Guélou, R., Eyma, F., Cantarel, A., Rivallant, S. and Castanié, B. (2022), "Dynamic crushing of wood-based sandwich composite tubes", *Mech. Adv. Mater. Struct.*, **29**(27), 7004-7024. https://doi.org/10.1080/15376494.2021.1991533

He, H., Shuang, E., Ai, L., Wang, X., Yao, J., He, C. and Cheng, B. (2023), "Exploiting machine learning for controlled synthesis of carbon dots-based corrosion inhibitors", *J. Cleaner Product.*, **419**, p. 138210. https://doi.org/10.1016/j.jclepro.2023.138210

Jangid, R.S. (2022), "Optimum parameters and performance of tuned mass damper-inerter for base-isolated structures", *Smart Struct. Syst.*, *Int. J.*, **29**(4), 549-560. https://doi.org/10.12989/sss.2022.29.4.549

Khandelwal, R.P., Chakrabarti, A. and Bhargava, P. (2019), "Efficient 2d thermo-mechanical analysis of composites and sandwich laminates", *Mech. Adv. Mater. Struct.*, **26**(6), 526-538. https://doi.org/10.1080/15376494.2017.1410897

Mahesh, V. (2022), "Nonlinear free vibration of multifunctional sandwich plates with auxetic core and magneto-electro-elastic facesheets of different micro-topological textures: fe approach", *Mech. Adv. Mater. Struct.*, **29**(27), 6266-6287. https://doi.org/10.1080/15376494.2021.1974619

Palomba, G., Epasto, G. and Crupi, V. (2022), "Lightweight sandwich structures for marine applications: a review", *Mech. Adv. Mater. Struct.*, **29**(26), 4839-4864. https://doi.org/10.1080/15376494.2021.1941448

Rechdaoui, M., Azrar, L., Belouettar, S., Daya, E. and Potier-Ferry, M. (2009), "Active vibration control of piezoelectric sandwich beams at large amplitudes", *Mech. Adv. Mater. Struct.*, **16**(2), 98-109. https://doi.org/10.1080/15376490802543691

Shirbhate, P. and Goel, M. (2023), "Investigation of effect of perforations in honeycomb sandwich structure for enhanced blast load mitigation", *Mech. Adv. Mater. Struct.*, **30**(17), 3463-3478. https://doi.org/10.1080/15376494.2022.2076958

Solak, A. (2024), "Bioinspired honeycomb sandwich structures for enhanced hail impact resistance", *Mech. Adv. Mater. Struct.*, 1-9. https://doi.org/10.1080/15376494.2024.2341303

Susainathan, J., Eyma, F., De Luycker, E., Cantarel, A. and Castanié, B. (2020), "Numerical modeling of impact on wood-based sandwich structures", *Mech. Adv. Mater. Struct.*, **27**(18), 1583-1598. https://doi.org/10.1080/15376494.2018.1519619

Tomlinson, H., Rodgers, G.W., Xu, C., Avot, V., Zhou, C. and Chase, J.G. (2023), "Accuracy and robustness of hysteresis loop analysis in the identification and monitoring of plastic stiffness for highly nonlinear pinching structures", *Smart Struct. Syst.*, *Int. J.*, **31**(2), 101-111. https://doi.org/10.12989/sss.2023.31.2.101

Wang, X., Wang, T., Lv, H., Wang, H. and Zeng, F. (2024), "Analytical modeling and experimental verification of a multi-DOF spherical pendulum electromagnetic energy harvester", *Energy*, **286**, p. 129428. https://doi.org/10.1016/j.energy.2023.129428

Wang, X., Cui, M., Li, W. and Gao, M. (2025), "Topology optimization of structures with steady-state heat conduction using an improved parameterized level set method", *Mech. Adv. Mater. Struct.*, 1-18. https://doi.org/10.1080/15376494.2025.2459358

Xin, Y., Yan, H., Yang, S., Li, H. and Cheng, S. (2021), "Experimental study on the indentation of epoxy resin–aluminum honeycomb composite sandwich panel", *Mech. Adv. Mater. Struct.*, **28**(9), 904-918. https://doi.org/10.1080/15376494.2019.1605009

Yang, L., Zappino, E., Carrera, E. and Du, J. (2024), "Rotation effects on propagation of shear horizontal surface waves in piezomagnetic-piezoelectric semiconductor layered structures", *Appl. Mathe. Modell.*, **129**, 494-508. https://doi.org/10.1016/j.apm.2024.02.020

Zappino, E., Najd, J., Carrera, E., Harizi, W. and Aboura, Z. (2024), "A global-local modelling approach for wave propagation, shm and damage detection in reinforced panels using integrated piezoelectric sensors", *Presented at the ASME Aerospace Structures*, *Structural Dynamics*, *and Materials Conference*, *American Society of Mechanical Engineers*, Vol.

87745, p. V001T01A018. https://doi.org/10.1115/SSDM2024-121613

Zhong, T., Feng, X., Zhang, Y. and Zhou, J. (2022), “Experimental study on the effect of ec-tmd on the vibration control of plant structure of pspps”, *Smart Struct. Syst., Int. J.*, **29**(3), 457-473. https://doi.org/10.12989/sss.2022.29.3.457

HJ

Appendix

The nomenclature table excerpt is presented in Table A.

Table A Nomenclature table excerpt

Symbol	Unit	Description
m	kg	Proof mass
k	N/m	Spring stiffness
c	$N \cdot s/m$	Mechanical damping coefficient
B	T	Magnetic flux density
N	$-$	Number of coil turns
R_c	Ω	Coil resistance
Θ	N/V	Piezoelectric coupling coefficient
C_p	F	Piezoelectric capacitance
ζ	$-$	Damping ratio